Edge Fracture in Complex Fluids

Ewan J. Hemingway, Halim Kusumaatmaja, and Suzanne M. Fielding
Department of Physics, Durham University, Science Laboratories, South Road, Durham DH1 3LE, United Kingdom
(Received 14 March 2017; published 14 July 2017)

We study theoretically the edge fracture instability in sheared complex fluids, by means of linear stability analysis and direct nonlinear simulations. We derive an exact analytical expression for the onset of edge fracture in terms of the shear-rate derivative of the fluid's second normal stress difference, the shear-rate derivative of the shear stress, the jump in shear stress across the interface between the fluid and the outside medium (usually air), the surface tension of that interface, and the rheometer gap size. We provide a full mechanistic understanding of the edge fracture instability, carefully validated against our simulations. These findings, which are robust with respect to choice of rheological constitutive model, also suggest a possible route to mitigating edge fracture, potentially allowing experimentalists to achieve and accurately measure flows stronger than hitherto possible.

DOI: 10.1103/PhysRevLett.119.028006

Rheology is the study of the deformation and flow of matter. In the most common rheological experiment, a sample of complex fluid—e.g., polymer, surfactant, or colloid—is sandwiched between plates and sheared (Fig. 1). Plotting the steady-state shear stress σ as a function of imposed shear rate $\dot{\gamma}$ then gives the flow curve $\sigma(\dot{\gamma})$, which plays a central role in characterizing any fluid's flow response. Almost ubiquitously encountered beyond a certain (material and device dependent) shear rate, however, is the phenomenon of edge fracture: the free surface where the fluid sample meets the outside air destabilizes (Fig. 1, right), rendering accurate rheological measurement impossible. This has been studied experimentally in Refs. [1–7] and cited as "the limiting factor in rotational rheometry" [6]. From a fluid-mechanical viewpoint, it is an important example of a hydrodynamic instability in free surface viscoelastic flow [3,8,9].

Despite this ubiquity, edge fracture remains poorly understood theoretically. Important early papers by Tanner and co-workers [10,11] predicted it to occur for a critical magnitude $|N_2(\dot{\gamma})| > \Gamma/R$ of the second normal stress difference N_2 in the fluid (we define N_2 below), given a surface tension Γ of the fluid-air interface and an assumed geometrical length scale R. This prediction was based on some key assumptions that will in fact prove inconsistent with our simulations. Taken as a scaling argument, however, it showed remarkable early insight.

The contributions of this Letter are fourfold. First, we show that the threshold for the onset of edge fracture is in fact set by $\Delta\sigma|N_2|'(\dot{\gamma})/\sigma'(\dot{\gamma}) > 2\pi\Gamma/L_y$, where prime denotes differentiation with respect to $\dot{\gamma}$, $\Delta\sigma$ is the jump in shear stress across the interface between the fluid and the outside air, and L_y is the gap size. (For a note on signs, see [12].) For low flow rates and negligible air viscosity, setting also $R = L_y$, Tanner's prediction happens to equal ours to within an $O(1)$ factor, despite containing fundamentally different physics. Second, we offer the first mechanistic understanding of edge fracture. Third, we predict the growth rate at which it develops for any imposed shear rate. Finally, we suggest a recipe by which it might be mitigated, potentially enabling experimentalists to achieve flows stronger than hitherto possible.

Our approaches comprise linear stability analysis and direct nonlinear simulation. At low shear rates in a simplified theoretical geometry [13], defined below, we obtain exact expressions for the threshold, eigenvalue, and eigenfunction for the onset of edge fracture, and show these to agree with counterpart nonlinear simulations. We further show this simplified geometry to closely predict onset in the experimentally realizable geometry of shear between plates.

As shown in Fig. 1 (right), we consider a planar slab of fluid sheared at rate $\dot{\gamma}$ with flow direction $\hat{\mathbf{x}}$ and flow-gradient direction $\hat{\mathbf{y}}$. For a small cone angle and large radius in the flow cell sketched in Fig. 1 (left), which is usually the case experimentally, this planar cartoon provides an excellent approximation. The edges of the sample in the vorticity direction $\hat{\mathbf{z}}$ are in contact with the air, with a sample length in that direction (initially, at the cell midheight $y = 0$)

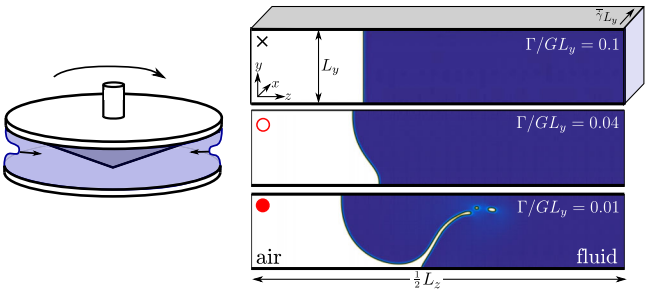

FIG. 1. Left: Schematic of a cone and plate device. Right: Snapshots from full nonlinear simulations of the Giesekus model between hard walls. $\dot{\gamma}\tau = 1.0$, $\theta = 90°$, $\alpha = 0.4$, and $\eta_a/G\tau = 0.01$.

denoted Λ. We assume translational invariance in $\hat{\mathbf{x}}$, performing two-dimensional simulations in the $y-z$ plane. Our simulation box has length L_z and periodic boundary conditions in z. Only its left half is shown in Fig. 1.

In the y direction we consider two different kinds of boundary condition. The first models the experimentally realizable case of shear between hard walls at $y = \pm L_y/2$, with no slip or permeation. The second gives the simplified biperiodic Lees-Edwards geometry, in which all quantities repeat periodically across shear-mapped points on the boundaries of box copies stacked in y, but with adjacent copies moving relative to each other at velocity $\dot{\gamma} L_y \hat{\mathbf{x}}$. Our numerically obtained threshold for the onset of edge fracture will prove in excellent agreement between these two. The simplified geometry allows analytical progress that is otherwise prohibitive.

The total stress $\mathbf{T}$ in any fluid element comprises an isotropic contribution $-p\mathbf{I}$ with pressure p, a Newtonian solvent contribution of viscosity η_s, and a viscoelastic contribution $\boldsymbol{\Sigma}$ from the complex fluid (polymer chains, emulsion droplets, etc.), with a scale set by a constant modulus G. We assume creeping flow conditions, giving the force balance condition $\nabla \cdot \mathbf{T} = 0$, and therefore $\eta_s \nabla^2 \mathbf{v} + \nabla \cdot \boldsymbol{\Sigma} - \nabla p = 0$ inside the fluid and $\eta_a \nabla^2 \mathbf{v} - \nabla p = 0$ in the air, with air viscosity η_a. The pressure field $p(\mathbf{r}, t)$ is determined by enforcing incompressibility, with the flow velocity $\mathbf{v}(\mathbf{r}, t)$ obeying $\nabla \cdot \mathbf{v} = 0$. The dynamics of $\boldsymbol{\Sigma}$ is determined by a viscoelastic constitutive equation of the form

$$\partial_t \boldsymbol{\Sigma} + \mathbf{v} \cdot \nabla \boldsymbol{\Sigma} = 2G\mathbf{D} + \mathbf{f}(\boldsymbol{\Sigma}, \nabla \mathbf{v}) - \frac{1}{\tau}\mathbf{g}(\boldsymbol{\Sigma}), \qquad (1)$$

where $\mathbf{D} = \frac{1}{2}(\nabla \mathbf{v} + \nabla \mathbf{v}^T)$. The first two terms on the rhs capture the loading of viscoelastic stress in flow, and the third represents the relaxation back towards an unstressed state. The forms of $\mathbf{f}$ and $\mathbf{g}$ prescribe the precise model, and we shall simulate in what follows the Johnson-Segalman [14] and Giesekus [15] models, set out in [16]. In the former, $\mathbf{f}$ contains a slip parameter a. In the latter, $\mathbf{g}$ contains an anisotropy parameter α. Importantly, however, our predictions for edge fracture will depend on a or α only via their appearance in the shear stress $\sigma \equiv T_{xy}$ and second normal stress difference $N_2 \equiv T_{yy} - T_{zz}$. In this way, the key physics proves robust to choice of constitutive model. Indeed, most complex fluids show the low-shear scalings $\sigma \sim \dot{\gamma}, N_2 \sim -\dot{\gamma}^2$ of this model. An exception are non-Brownian suspensions [23], deferred to future work.

Our simulations model the air-fluid coexistence by a Cahn-Hilliard equation [16,24,25], with a mobility M for air-fluid intermolecular diffusion, a scale G_μ for the free energy density of demixing, and a slightly diffuse air-fluid interface of thickness l, with surface tension $\Gamma = 2\sqrt{2} G_\mu l/3$. Our linear stability analysis assumes a sharp interface, with a surface tension Γ. Our results for these two approaches agree fully.

In unsheared equilibrium, the contact angle where the air-fluid interface meets the flow cell walls is denoted θ. A value $\theta = 90°$ gives a vertical equilibrium interface, $\theta > 90°$ an interface convex into the air, and $\theta < 90°$ concave. In having a diffuse interface [25], our simulations capture any motion of the contact line along the wall in flow. In the simplified biperiodic geometry the equilibrium interface is always vertical, mimicking $\theta = 90°$ with walls. As the initial condition for our shear simulations, we take a coexistence state first equilibrated without shear, with a small perturbation then added to the interface's position $h(y)$ along the z axis, $h \to h + 10^{-8}\cos(n\pi y/L_y)$, to trigger edge fracture, taking $n = 1$ with walls and $n = 2$ in the biperiodic geometry.

Important dimensionless quantities that we shall explore are the scaled surface tension Γ/GL_y, the Weissenberg number $\dot{\gamma}\tau$, the equilibrium contact angle θ, and the air viscosity $\eta_a/G\tau$. Less important parameters, which do not affect the physics once converged to their physically appropriate large or small limit are the cell aspect ratio, $L_z/L_y = 10.0$, the air gap size $(L_z - \Lambda)/L_y = 3.0$, the small solvent viscosity [16], the air-fluid interface width $l/L_y = 0.01$, and the inverse mobility for intermolecular diffusion, $l^2/MG_\mu\tau = 0.01$–0.1.

We now present our results. The basic phenomenon is exemplified by the three late-time snapshots of our nonlinear simulations of the Giesekus model between hard walls in Fig. 1 (right). At any given imposed strain rate, an air-fluid interface with high surface tension is undisturbed by the flow and retains its equilibrium shape (top snapshot). We shall denote such states by a black cross in Fig. 2. For an intermediate surface tension the interface partially fractures, displacing in the z direction a distance $O(L_y)$ set by the gap between the rheometer plates in the y direction, before settling to a new steady-state shape, different from its unsheared equilibrium one. We denote

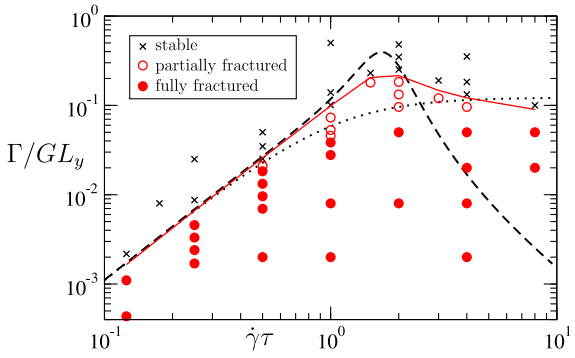

FIG. 2. Edge-fracture phase diagram for the Johnson-Segalman model in Lees-Edwards biperiodic shear. Solid line: phase boundary between stable and partially fractured states. Dashed line: prediction of Eq. (8), with no adjustable parameters. Dotted line: Tanner's prediction, with the prefactor adjusted to best fit the simulations in the limit $\dot{\gamma}\tau \to 0$. $a = 0.3$ and $\eta_a/G\tau = 0.01$.

these states by red open circles. Finally, for a low surface tension, the interface fully fractures, displacing in the z direction a distance $O(\Lambda)$ set by the sample width in that direction (red closed circles). Here the system never attains a new steady state: depending on the wetting angle and flow rate, the fluid may, e.g., dewet the wall, and/or air bubbles may invade the fluid.

In Fig. 2, we collect into a phase diagram the results of simulations at many values of surface tension and shear rate, for the Johnson-Segalman model in the biperiodic geometry. (In the Supplemental Material [16], we show that the phase boundary is essentially independent of model, geometry, and equilibrium wetting angle θ.) The red solid line marks the phase boundary between undisturbed and partially fractured interfacial states.

Within the biperiodic geometry, we now perform a linear stability analysis to derive an expression for this onset threshold, in the limit of low strain rates. To do so, we represent the state of the system as an underlying homogeneous time-independent base state (denoted by subscript 0), corresponding to the initially unfractured case in which the interface is flat and the flow uniform. (Recall that our nonlinear simulations showed the phase boundary to be independent of the initial interfacial shape [16].) To this, we add a small perturbation (denoted by overtildes) representing the precursor of edge fracture. For any given interfacial tension Γ and imposed flow rate $\dot\gamma$, we then determine whether the perturbation grows towards an edge-fractured state, or decays to leave a flat interface.

Accordingly, in the fluid bulk we write the velocity field $\mathbf{v} = \mathbf{v}_0 + \tilde{\mathbf{v}} = (\dot\gamma y, 0, 0) + (\tilde v_x, \partial_z\tilde\psi, -\partial_y\tilde\psi)$ and stress field $\mathbf{T} = \mathbf{T}_0 + \tilde{\mathbf{T}}$. Our use of a stream function $\tilde\psi$ automatically ensures incompressibility. The force balance condition $\nabla\cdot\mathbf{T} = 0$ then simply becomes $\nabla\cdot\tilde{\mathbf{T}} = 0$. In the fluid bulk the x component of force balance and the curl of its y, z components are, respectively,

$$0 = \partial_y\tilde T_{xy} + \partial_z\tilde T_{xz}, \tag{2a}$$

$$0 = \partial_y\partial_z(\tilde T_{yy} - \tilde T_{zz}) + (\partial_z^2 - \partial_y^2)\tilde T_{yz}. \tag{2b}$$

We likewise write the z position of the interface at any gap coordinate y as $h_0 + \tilde h(y)$. We further choose the origin of z to lie at the interface, so $h_0 = 0$, with fluid for $z > 0$ and air for $z < 0$. The condition of force balance $\mathbf{n}\cdot\mathbf{T} + \Gamma\mathbf{n}\nabla_{\rm int}\cdot\mathbf{n} = 0$ across this perturbed interface with normal $\mathbf{n} = \hat{\mathbf{z}} - \partial_y\tilde h\,\hat{\mathbf{y}}$ and $\nabla_{\rm int}$ the interfacial gradient operator gives componentwise linearized equations

$$0 = \tilde T_{xz}|_{z=0^+} - \Delta\sigma\partial_y h, \tag{3a}$$

$$0 = \tilde T_{yz}|_{z=0^+} - N_2\partial_y h, \tag{3b}$$

$$0 = \tilde T_{zz}|_{z=0^+} + \Gamma\partial_y^2 h, \tag{3c}$$

with $\Delta\sigma$ and N_2 the jumps in the shear and second normal stress difference across the interface, from fluid to air. (N_2 is always zero in the air, so we omit its Δ prefix.) Note we have assumed (for now) negligible stresses on the air side of the interface, $z = 0^-$. The interface moves with the z component of the fluid velocity,

$$\partial_t\tilde h = -\partial_y\tilde\psi|_{z=0}. \tag{4}$$

Finally, we must specify the perturbed stress components $\tilde T_{ij}$ in Eqs. (2) and (3). Each comprises a solvent contribution of viscosity η_s and a viscoelastic stress that follows Eq. (1). For values of $(\Gamma/GL_y, \dot\gamma\tau)$ only just across the instability threshold in Fig. 2, the interface will destabilize only very slowly and the viscoelastic stress will, for any instantaneous interfacial shape, be determined as the quasistatic solution of Eq. (1). In the limit of small imposed shear rate $\dot\gamma$, this gives

$$\tilde T_{xy} = (G\tau + \eta_s)\partial_y\tilde v_x + O(\dot\gamma), \tag{5a}$$

$$\tilde T_{xz} = G\tau + \eta_s)\partial_z\tilde v_x + O(\dot\gamma), \tag{5b}$$

$$\tilde T_{yy} - \tilde T_{zz} = 4(G\tau + \eta_s)\partial_y\partial_z\tilde\psi - 2\dot\gamma G\tau^2 b\partial_y\tilde v_x, \tag{5c}$$

with $b = 1 - a$ and α in the Johnson-Segalman and Giesekus models, respectively.

Substituting Eq. (5) (with a counterpart expression for $\tilde T_{yz}$) into Eqs. (2) and (3) gives finally a set of coupled partial differential equations for the perturbation to the bulk flow field, $\tilde v_x(y,z,t), \tilde\psi(y,z,t)$, and to the interface position $\tilde h(y,t)$. Solving these gives, to leading order in $\dot\gamma$ and at any wave vector q in the y direction,

$$\begin{aligned}\tilde\psi(y,z,t) &= [Ae^{-qz} + Be^{-kz}]e^{iqy}e^{\omega t},\\ \tilde v_x(y,z,t) &= Ce^{-qz}e^{iqy}e^{\omega t},\\ \tilde h(y,t) &= iqDe^{iqy}e^{\omega t}\end{aligned} \tag{6}$$

(ignoring a small term in e^{-kz} in $\tilde v_x$), in which $k = q/\sqrt{1+\beta}$ with $\beta \approx b(1-b)\dot\gamma^2\tau^2$, and with known expressions for A, B, C, D that we do not write. These eigenfunctions $\tilde\psi(y,z)$, $\tilde v_x(y,z)$ are shown in the left panel of Fig. 3 and agree fully with their counterparts from (the linear regime of) our fully nonlinear simulations in the same panel.

Equation (6) tells us that perturbations at any wave vector q will grow if their eigenvalue $\omega(q) > 0$. We find

$$\omega = \frac{1}{2(G\tau + \eta_s)}\left(\frac{1}{2}\Delta\sigma\frac{d|N_2|}{d\dot\gamma}\Big/\frac{d\sigma}{d\dot\gamma} - \Gamma q\right). \tag{7}$$

The condition $\omega > 0$ is most readily satisfied for the mode with the lowest wave vector that is consistent with the boundary conditions, $q = 2\pi/L_y$. Accordingly, our final

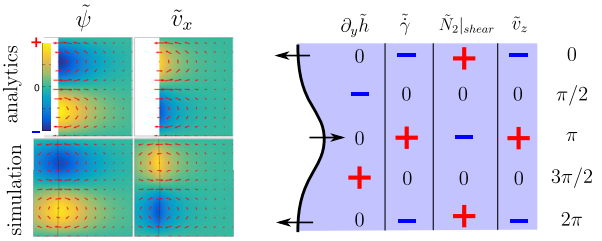

FIG. 3. Left: Eigenfunctions from analytic calculation (top) and simulation (bottom). (Analytics ignore the air phase, as shown by the white regions.) $\dot{\gamma}\tau = 0.125$, $a = 0.3$, $\Gamma/GL_y = 0.0$, $\eta_a/G\tau = 0.01$, and $q = 2\pi/L_y$. Right: Instability mechanism, discussed in text, with 0 and $\pm$ symbols corresponding to the phase locations shown.

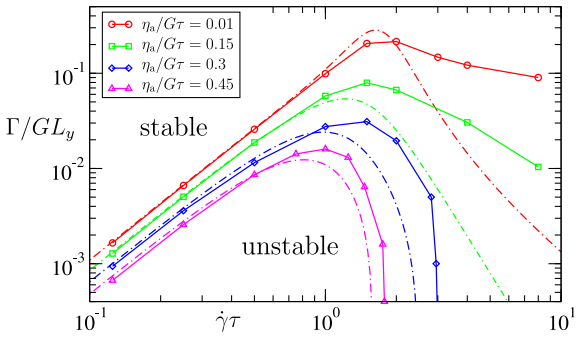

FIG. 4. Threshold for onset of edge fracture instability in the Johnson-Segalman model in biperiodic shear, for various values of the viscosity η_a of the bathing medium. Solid lines: full nonlinear simulation. Dotted lines: linear stability analysis, valid in the limit $\dot{\gamma}\tau \to 0$. $a = 0.3$ and $\eta_s/G\tau = 0.15$.

condition for an initially flat fluid-air interface to undergo edge fracture is given by

$$\frac{1}{2}\Delta\sigma\frac{d|N_2(\dot{\gamma})|}{d\dot{\gamma}}\Big/\frac{d\sigma}{d\dot{\gamma}} > \frac{2\pi\Gamma}{L_y}. \tag{8}$$

This criterion is marked by the dashed line in Fig. 2, and fully agrees at low shear rates with the onset of fracture in our numerical simulations.

We now compare Eq. (8) with Tanner's prediction of $|N_2| > 2\Gamma/3R$, with R the radius of an assumed initially semicircular interfacial crack. Clearly, R must now be replaced by the dominant wavelength L_y. Disregarding $O(1)$ prefactors, the important difference between Tanner's prediction and ours then lies in replacing

$$|N_2| \to \frac{1}{2}\Delta\sigma\frac{d|N_2|}{d\dot{\gamma}}\Big/\frac{d\sigma}{d\dot{\gamma}}. \tag{9}$$

Given negligible air viscosity, the jump $\Delta\sigma$ in shear stress across the interface between the fluid and air simply equals the shear stress σ in the fluid. For most complex fluids (excluding non-Brownian suspensions), in the limit of small shear rates, $N_2 \sim -\dot{\gamma}^2$ and $\sigma \sim \dot{\gamma}$. Tanner's $|N_2|$ on the lhs of Eq. (9) then simply equals our expression on the rhs. In contrast, at higher shear rates these simple power laws no longer (in general) hold, and our prediction departs from Tanner's, as seen in Fig. 2. Indeed, Tanner predicts the critical surface tension to increase monotonically with shear rate. The nonmonotonicity that we find follows because σ and $|N_2|$ both initially increase with $\dot{\gamma}$, before $N_2(\dot{\gamma})$ saturates to a constant at high shear rates, such that $dN_2/d\dot{\gamma} \to 0$.

Our results also explain the mechanism of instability as follows. Were the interface to remain perfectly flat, the jump $\Delta\sigma$ in shear stress across it would be consistent with force balance. However, any small interfacial tilt $\partial_y\tilde{h}$ (first column of Fig. 3, right) exposes this jump. To maintain force balance across the interface, a counterbalancing perturbation $\tilde{T}_{xz} = iqh\Delta\sigma$ is then required [Eq. 3(a)]. To maintain the x component of force balance in the fluid bulk [Eq. 2(a)], a corresponding perturbation $\tilde{T}_{xy}$ is then needed, achieved via a perturbation $\tilde{\dot{\gamma}} = \partial_y\tilde{v}_x = qh\Delta\sigma/\sigma'(\dot{\gamma})$ in the shear rate (second column of Fig. 3, right). The second normal stress $N_2 \approx -bG\tau^2\dot{\gamma}^2$ in the fluid bulk then suffers a corresponding perturbation [second term in Eq. (5c)] $\tilde{T}_{yy} - \tilde{T}_{zz}|_{\rm shear} = -qh\Delta\sigma|N_2|'(\dot{\gamma})/\sigma'(\dot{\gamma})$ (third column of Fig. 3, right). This must be counterbalanced (at zero surface tension at least) by an equal and opposite extensional perturbation [first term in Eq. (5c)] $\tilde{T}_{yy} - \tilde{T}_{zz}|_{\rm ext} = 4G\tau\partial_y\partial_z\tilde{\psi} = -4G\tau\partial_z\tilde{v}_z = 4G\tau q\tilde{v}_z$. This requires a z component of fluid velocity (fourth column of Fig. 3, right), which convects the interface, $\partial\tilde{h}/\partial t = \tilde{v}_z = \frac{1}{4}\Delta\sigma h|N_2|'(\dot{\gamma})/G\tau\sigma'(\dot{\gamma})$, enhancing its original tilt with a growth rate $\omega = \frac{1}{4}\Delta\sigma|N_2|'(\dot{\gamma})/G\tau\sigma'(\dot{\gamma})$, consistent with Eq. (7) at zero surface tension, noting that η_s is small. This mechanism resembles in spirit that of instabilities between layered viscoelastic fluids [26–28].

Finally, our results suggest a recipe via which edge fracture might be mitigated. By immersing the flow cell in an immiscible Newtonian "bathing fluid" with a viscosity larger than that of air, more closely matched to that of the study fluid, the jump $\Delta\sigma$ in shear stress between the study and bathing fluids, which is a key factor in driving the instability, will be reduced. This is explored in Fig. 4. The red solid line shows the onset threshold for a bathing fluid of negligible viscosity, such as air, and the green, blue and magenta lines for successively increasing values of the bathing fluid's viscosity, each giving increased stability. The dashed lines show linear stability results recalculated with nonzero bath viscosity, in excellent agreement. Clearly, choosing a bathing fluid with as a high a possible surface tension with the test fluid will also help stability.

To summarize, we have derived an exact expression for the onset of edge fracture in complex fluids, shown it to agree with numerical simulations, and provided the first mechanistic understanding of edge fracture. We have also suggested a way of mitigating the phenomenon

experimentally. Given the status of edge fracture as a crucially limiting factor in experimental rheology, this suggests a route to accessing flows stronger than hitherto possible.

The research leading to these results has received funding from the European Research Council under the EU's 7th Framework Programme (FP7/2007–2013), ERC Grant No. 279365. The authors thank Peter Olmsted for discussions and Mike Cates and Roger Tanner for critical readings of the manuscript.

[1] C. S. Lee, B. C. Tripp, and J. J. Magda, Rheol. Acta **31**, 306 (1992).
[2] Y. W. Inn, K. F. Wissbrun, and M. M. Denn, Macromolecules **38**, 9385 (2005).
[3] C. Sui and G. B. McKenna, Rheol. Acta **46**, 877 (2007).
[4] T. Schweizer and M. Stockli, J. Rheol. **52**, 713 (2008).
[5] K. M. Mattes, R. Vogt, and C. Friedrich, Rheol. Acta **47**, 929 (2008).
[6] E. A. Jensen and J. d. C. Christiansen, J. Non-Newtonian Fluid Mech. **148**, 41 (2008).
[7] S.-C. Dai, E. Bertevas, F. Qi, and R. I. Tanner, J. Rheol. **57**, 493 (2013).
[8] J. Eggers and E. Villermaux, Rep. Prog. Phys. **71**, 036601 (2008).
[9] G. H. McKinley, in *Annual Rheology Reviews*, edited by D. M. Binding and K. Walters (British Society for Rheology, Aberystwyth, 2005), pp. 1–48.
[10] R. I. Tanner and M. Keentok, J. Rheol. **27**, 47 (1983).
[11] M. Keentok and S.-C. Xue, Rheol. Acta **38**, 321 (1999).
[12] We consider throughout positive flow rates, $\dot{\gamma} > 0$. For negative flow rates we must replace $d|N_2|/d\dot{\gamma}$ by $d|N_2|/d|\dot{\gamma}|$. For most fluids $N_2(\dot{\gamma}) \sim -\dot{\gamma}^2$.
[13] A. Onuki, J. Phys. Soc. Jpn. **66**, 1836 (1997).
[14] M. Johnson and D. Segalman, J. Non-Newtonian Fluid Mech. **2**, 255 (1977).
[15] H. Giesekus, J. Non-Newtonian Fluid Mech. **11**, 69 (1982).
[16] See Supplemental Material at http://link.aps.org/supplemental/10.1103/PhysRevLett.119.028006 for a definition of the models used, a discussion on the robustness of our results with respect to boundary condition and choice of model, and details of the numerical implementation, which includes Refs. [14,15,17–22].
[17] S. Skorski and P. D. Olmsted, J. Rheol. **55**, 1219 (2011).
[18] A. Bray, Adv. Phys. **43**, 357 (1994).
[19] P. Yue, C. Zhou, and J. J. Feng, J. Fluid Mech. **645**, 279 (2010).
[20] S. Dong, Comput. Methods Appl. Mech. Eng. **247–248**, 179 (2012).
[21] C. Pozrikidis, *Introduction to Theoretical and Computational Fluid Dynamics* (Oxford University Press, New York, 2011).
[22] W. H. Press, S. A. Teukolsky, W. T. Vetterling, and B. P. Flannery, *Numerical Recipes in C: The Art of Scientific Computing*, 2nd ed. (Cambridge University Press, Cambridge, England, 1992).
[23] M. M. Denn and J. F. Morris, Annu. Rev. Chem. Biomol. Eng. **5**, 203 (2014).
[24] D. M. Anderson, G. B. McFadden, and A. A. Wheeler, Annu. Rev. Fluid Mech. **30**, 139 (1998).
[25] H. Kusumaatmaja, E. J. Hemingway, and S. M. Fielding, J. Fluid Mech. **788**, 209 (2016).
[26] E. Hinch, O. Harris, and J. M. Rallison, J. Non-Newtonian Fluid Mech. **43**, 311 (1992).
[27] H. J. Wilson and J. M. Rallison, J. Non-Newtonian Fluid Mech. **72**, 237 (1997).
[28] S. M. Fielding, Phys. Rev. Lett. **104**, 198303 (2010).